Research Square

Preprints are preliminary reports that have not undergone peer review.
They should not be considered conclusive, used to inform clinical practice,
or referenced by the media as validated information.

Recovery time and exposure for six harmonized extreme climate event categories under global warming

Karim Zantout

karim.zantout@pik-potsdam.de

Potsdam Institute for Climate Impact Research, Potsdam, Germany https://orcid.org/0000-0002-1357-1721

Dánnell Quesada-Chacón

Potsdam Institute for Climate Impact Research, Potsdam, Germany https://orcid.org/0000-0001-5700-1846

Sandra Zimmermann

Potsdam Institute for Climate Impact Research, Potsdam, Germany https://orcid.org/0009-0005-0130-0528

Jan Volkholz

Potsdam Institute for Climate Impact Research, Potsdam, Germany https://orcid.org/0000-0002-2533-3739

Katja Frieler

Potsdam Institute for Climate Impact Research, Potsdam, Germany https://orcid.org/0000-0003-4869-3013

Jacob Schewe

Potsdam Institute for Climate Impact Research, Potsdam, Germany https://orcid.org/0000-0001-9455-4159

Research Article

Keywords: climate extreme events, climate scenarios, recovery times, crop failure, drought, heat wave, flood, tropical cyclone, wildfire

Posted Date: March 6th, 2026

DOI: https://doi.org/10.21203/rs.3.rs-9039183/v1

License: This work is licensed under a Creative Commons Attribution 4.0 International License.
Read Full License

Additional Declarations: The authors declare no competing interests.

Recovery time and exposure for six harmonized extreme climate event categories under global warming

Karim Zantout[1,2,*], Dánnell Quesada-Chacón[1], Sandra Zimmermann[1], Jan Volkholz[1], Katja Frieler[1], and Jacob Schewe[1]

[1]*Potsdam Institute for Climate Impact Research, Potsdam, Germany*
[2]*Karlsruhe University of Applied Sciences, Karlsruhe, Germany*
[*]*Corresponding author: Karim Zantout, karim.zantout@pik-potsdam.de*

March 5, 2026

Abstract

Climate variability gives rise to different extreme events, including crop failure, drought, flood, heatwave, tropical cyclone, and wildfire. The temporal and spatial characteristics of these events have already begun to shift, and are expected to change further under continued global warming. In studies of climate change impacts, different types of events are often studied in isolation. However, locations exposed to extreme events are typically not only affected by a single extreme event category. We therefore quantify exposure and mean recovery times for six different extreme event types on a $0.5^\circ \times 0.5^\circ$ global grid under historical and projected future climates. We use harmonized ensembles of global biophysical impact simulations driven with (i) bias-adjusted climate data, to assess current conditions, and (ii) climate model projections, to quantify future changes in recovery times. While we observe a decrease in global mean recovery time as a function of warming level across all event types, the decrease rates differ strongly between event types ranging from constant to flattening rates. Being able to quantify the temporal evolution of recovery times is crucial for disaster planning and adaptation or relocation efforts.

1 Introduction

Extreme climate events that are further aggravated by anthropogenic climate change have detrimental effects on human societies and ecosystems [1–3]. For example, 2 million deaths and 3.6 trillion US$ of economic loss between 1970 and 2019 are caused globally by natural disasters [4]. In addition, weather-related natural disasters are responsible for 45.5 million new internal displacements in 2024 [5].

Many studies have investigated the changing intensity and frequency of extreme climate events showing heterogeneous geographical and temporal effects [2, 3, 6–9]. While results show consistent trends it is apparent that sensitivities arise from the underlying models and extreme event definitions [10–13]. For example, climate change affects 100-year river floods qualitatively different compared to 20-years floods [14]. Given that most world regions are affected by more than one extreme event type, e.g. heatwave and wildfire, we develop future scenarios on a common basis for all extreme event categories. A better understanding of the geography and temporal dynamics across different extreme event categories is essential for insurances, adaptation planning and the respective resource allocation. In addition, the mean recovery time from extreme events is important to identify critical thresholds for affected ecosystems, namely when the mean recovery time from extreme climate

events is smaller than typical recovery times of ecosystems [15, 16]. For example, forest regeneration requires enough recovery time between severe fires and therefore exhibits critical thresholds in terms of the recovery time [17, 18].

To provide the underlying comparability among different extreme event scenarios, the Inter-Sectoral Impact Model Intercomparison Project (ISIMIP) offers a common modeling protocol across different sectors, such as agriculture, water, and biomes [19–21]. The resulting climate impact simulations were previously used to develop scenarios for extreme climate events across six different categories, namely crop failure, drought, flood, heatwave, tropical cyclone, and wildfire [2]. To the knowledge of the authors the dataset in Ref. [2] is unique in terms of variety of extreme event categories and consistency of modeling protocol. Nevertheless, the applied extreme event definitions are heterogeneous in the sense that the mean recovery time between two extreme events is different across the six categories for the common baseline scenario. This heterogeneity is useful to implement differences in the actual impact but limits the comparability of recovery times across extreme event categories.

In this work we develop extreme event scenarios based on the latest ISIMIP runs and homogeneous extreme event definitions for crop failure, drought, flood, heatwaves, tropical cyclone and wildfire. The resulting projections are used to quantify the change in mean recovery time under global warming and compare these across extreme event categories.

For crop failure previous studies have projected a reduction in mean recovery time by a factor of up to 4.5 by 2030 and 25 by 2050 across global breadbaskets for the RCP8.5 scenario [22] and a 4.2% reduction in crop production seasons per year by 2050 [23]. In the case of droughts global event frequency increased in 29% of global land areas compared to a historical baseline while spatially disaggregated results show a decline in drought frequency at high latitudes and increase in most other world regions spanning a range of factors from around 0.5 to 2 with respect to a historical baseline [24]. Extreme flood events show large regional heterogeneity and model uncertainty where predictions range from little change to increases by a factor of 10 in frequency due to global warming [25]. The frequency of heatwaves is also expected to increase by a factor of 2 to 3 for global warming at 2.5°C warming [26]. Similarly, for tropical cyclones the global consensus projection for category 4 and 5 tropical cyclone frequency in 2081–2100 shows an increase by 0 to 50% with respect to the 2000–2019 baseline [27, 28] where large deviations between models typically occur to intrinsic complexities such as tropical cyclone genesis, seeding etc. [29]. Due to historical warming the frequency of extreme fire weather was already observed to have increased by 54% with strong spatial heterogeneity while the frequency is projected to increase by 58% at 2°C and 104% at 3°C [30].

Socioeconomic conditions are important additional factors for the risk of climate extreme events that go beyond the mere hazard component [31–34]. As we are interested in quantifying the change of mean recovery time as a function of warming, we rely in this study on process-based and bias-corrected climate impact models from ISIMIP where socioeconomic variables are controllable [19, 20]. We fix socioeconomic parameters within these models to investigate temporal and geographical patterns that arise from natural processes such as temperature and precipitation variability, water circulation, and biomes growth dynamics. By keeping such condition constant at 2015 conditions we do not consider additional effects that arise from direct human influences, such as land and water management, and the uncertainties from socio-economic projections [35]. Moreover, the multi-model approach within ISIMIP allows to estimate the modeling uncertainty from single models given the harmonized inputs and consistent modeling protocols [19, 20]. We use global gridded time series data from ISIMIP Phase 3b to calculate the respective extreme event time series from 1850 to 2100 for three different SSP scenarios. The extreme events are consistently defined through percentiles of the respective pre-industrial extreme event indicator distribution (see details in Sec. 2). Note that our choice of extreme events includes not only climate impacts but also one direct meteorological hazard, namely heatwaves that are directly derived from temperature. This allows us to contrast the direct effect from global warming (heatwaves) to the additional effects as implemented within

process-based impact models (crop failure, drought, flood, tropical cyclone, and wildfire).

Our results show strong heterogeneity across mean recovery times as a function of warming. In the case of heatwave, drought, and wildfire we observe non-linear trends with strong decreases below 2°C while floods show a quasi-linear reduction in mean recovery time across a wide warming range of 0 to 4°C. On the other hand, crop failure and tropical cyclones show a reduction in mean recovery time but with a wide variation across models. This heterogeneity also extends to the geographical dimension where regional differences appear across event categories for the low warming SSP1-2.6 scenario.

2 Data and Methodology

2.1 Data

The data basis for our extreme event scenarios are climate simulations from ISIMIP [19–21] that are driven by bias-adjusted [36, 37] daily output of General Circulation Models (GCMs) from Phase 6 of the Coupled Model Intercomparison Project (CMIP6) [38, 39] (see Tab. 1). Here, we focus on the extreme event categories crop failure, drought, flood, heatwave, tropical cyclone, and wildfire which correspond to different climate impact sectors within ISIMIP, namely agriculture, biomes, fire, and water. While heatwave exposure is directly derived from the bias-adjusted GCM temperature output, the exposure to crop failure, flood, drought, tropical cyclone and wildfire relies on process-based crop, hydrological, hydrodynamical, tropical cyclone wind field, and vegetation model simulation results, respectively (see Tab. 1). The simulations consist of annual exposure time series from 1850 to 2100, whereby we distinguish a historical (1850–2014) and a future (2015–2100) period. For the future time period we rely on the Shared Socio-economic Pathways SSP1-2.6, SSP3-7.0 and SSP5-8.5 [39–41]. To compare the different scenarios to a baseline we run an additional scenario "piControl" which represents stable pre-industrial climate condition from 1850 to 2100 [20]. As different climate impact models run at different spatial resolutions we upscale the GCM, flood model, and tropical cyclone model simulations to a spatial resolution of 0.5° latitude and 0.5° longitude while the crop, drought and wildfire model simulations already have this resolution.

Extreme event exposure is determined both by the effects of physical and biogeochemical processes and socio-economic conditions. Due to the intricacies of socio-economic projections and our focus on natural process, we fix the socio-economic conditions in all impact models to the ones in 2015, e.g. land management and land use.

Crop failure results are derived from maize, rice, soybean, and rice yield estimates from 8 global gridded crop models (GGCMs; see Table 1), provided by AgMIP's Global Gridded Crop Model Intercomparison [11]. Note that some crop models distinguish between different wheat and rice types, e.g. winter and summer wheat, which we also account for in our analysis. We define a drought based on annual soil moisture within the upper soil layer to represent root moisture based on the hydrological models in Tab. 1. Since soil layers have different thicknesses across models we harmonize the soil moisture by summing it over a consistent number of layers to cover the root layer (see Supplementary Information Sec. 1).

Based on the global hydrological models (see Tab. 1) we use the global river routing model CaMa-Flood [42] to derive flood depths of floods that exceed a 40 year return interval. The return interval is derived from fitting a generalized extreme value distribution to the piControl annual maximum discharge time series. As a result we obtain global flood depth time series that align with a 40 year return interval.

Tropical cyclones tracks are simulated within a dynamical tropical cyclone model, as provided by WindRiskTech [43, 44], employing boundary conditions from GCMs, such as sea surface temperature, air temperature, and wind shear. Each GCM-experiment combination available, shown in Supplementary Information Tab. S2, yields 1500 tracks per year, which are then converted to wind

	impact model	global circulation model
crop failure	CROVER, CYGMA1p74, EPIC-IIASA, ISAM, LDNDC, LPJmL, PEPIC, PROMET	GFDL-ESM4, IPSL-CM6A-LR, MPI-ESM1-2-HR, MRI-ESM2-0, UKESM1-0-LL
drought	H08, JULES-W2, LPJmL-5-7-10-fire, WaterGAP2-2e, WEB-DHM-SG	
flood	H08, JULES-W2, LPJmL-5-7-10-fire, WaterGAP2-2e, WEB-DHM-SG	
heatwave	HWMId	
wildfire	CLASSIC*, LPJmL-5-7-10-fire, VISIT	
tropical cyclone	Holland08 (windfield model)	IPSL-CM6A-LR, MPI-ESM1-2-HR, MRI-ESM2-0, UKESM1-0-LL

Table 1: Table of climate and impact models for all extreme event categories. *Note that CLASSIC simulations are only available for GFDL-ESM4 and UKESM1-0-LL input.

speed fields using the Holland08 parametric wind model [45], at a spatial resolution of $0.1^\circ \times 0.1^\circ$. To obtain regionally representative statistics of tropical cyclones, the simulated windfields are bias-adjusted subbasin-wise against the windfields generated with the IBTrACS observational dataset [46]; a process which aims to correct biases in both landfall frequency and intensity of the simulated tropical cyclones. Since some GCM-experiment combinations do not provide simulated tracks for the full time period analysed in this study (see Tab. S2), we calibrate a statistical tool which employs global mean temperature (GMT) and El Niño Southern Oscillation (ENSO) index as predictors to draw samples of tropical cyclones for a given subbasin and year (with a given GMT and ENSO state). This process is similar to the one described in [47]. In this study, we generated 100 tropical cyclone realisations for each GCM, experiment, subbasin and year, using the statistical tool. For our extreme tropical cyclone definition we use the maximum annual wind speed above hurricane-force winds (64 knots according to the Saffir-Simpson scale) for each realisation.

Wildfire exposure is derived from the annual aggregate of burnt area output of global terrestrial biosphere models (see Tab. 1).

Note that we define the extreme events on an annual time scale while extreme climate events typically occur at shorter time scales. This approach allows to compare different extreme event categories on the same basis since, for example, droughts occur on longer time scales than tropical cyclones.

For each grid cell, crop type (maize, rice, soybean, and wheat), and irrigation type (irrigated and rainfed) we define a crop to fail if the crop yield falls below the 2.5th percentile of the respective piControl yield distribution. This threshold represents extreme events with a mean recovery time of 40 years. At each grid cell we calculate the sum of grid cell area fractions whereupon the crop type is grown which falls below the threshold. The binary crop failure exposure is one if the total failed grid cell area fraction is larger than 30% of the total crop area in that grid cell; otherwise, the crop failure exposure is zero. The percentile and area fraction criterion lead to an average global mean recovery times of 34 years under pre-industrial conditions (see Supplementary Material Tab. S4).

In the case of droughts we consider yearly soil moisture at root level (see Supplemental Material Sec. 1). If the annual soil moisture falls below the 2.5th percentile of the piControl distribution we consider the respective grid cell to be affected by drought in that year. The percentile threshold leads to an average global mean recovery time of 36 years (see Supplementary Material Tab. S4).

The flood definition is based on the flood depth as obtained by CaMa-Flood [42], namely a grid cell is affected by extreme flooding if the annual maximum flood depth is above the 97.5th percentile of the respective piControl distribution. Note that flood results are upscaled from $0.25^\circ \times 0.25^\circ$ resolution to $0.5^\circ \times 0.5^\circ$ to ensure consistency between extreme event categories. In the case of droughts and floods we additionally apply a drought mask to our results, removing all dry areas defined through an annual mean discharge below 0.1 mm/d. In the case of floods this acknowledges for the model bias where rivers are assumed to be everywhere. This flood definition leads to an average global mean recovery times of 37 years (see Supplementary Material Tab. S4).

We calculate heatwaves from near-surface air temperature based on the Heat Wave Magnitude Index daily (HWMId) [48, 49]. Specifically, we define a grid cell to be exposed to a heatwave if the HWMId of that year exceeds the 97.5th percentile of the piControl distribution of that grid cell. This heatwave definition leads to an average global mean recovery times of 36 years (see Supplementary Material Tab. S4).

Tropical cyclones are defined via 100 emulated tropical cyclone realizations under pre-industrial conditions. The threshold for tropical cyclones is determined by the 98.8th percentile of the sample maximum annual wind speed of the piControl distribution. In the case where this percentile threshold is below 64 knots wind speed, namely the threshold to qualify as a hurricane, we exclude these grid cells from the analysis (see Supplementary Information Sec. 1.3). We define a tropical cyclone if at least 4 out of the 100 emulated realizations exceed the threshold. The critical number of realizations was determined from the Binomial distribution using the independence of each realization since $P(X \geq 4) = 3.28\%$ and $P(X \geq 5) = 0.73\%$ for individual extreme event probability

$p = 100\% - 98.8\% = 1.2\%$ and number of realizations $n = 100$. While 3.28% is larger than 2.5% we chose this value to obtain a global mean recovery time of 35 years compensating for the small number of emulated realizations and leading to an extreme event definition that is consistent with the other categories (see Supplementary Material Tab. S4). Note that tropical cyclone results are upscaled from $0.1^\circ \times 0.1^\circ$ resolution to $0.5^\circ \times 0.5^\circ$ to ensure consistency between event types.

Finally, wildfires are defined through the annual burnt area as produced by the global vegetation models. A wildfire occurs in a grid cell if the yearly burnt area exceeds the 97.5th percentile of the respective piControl distribution. This wildfire definition leads to an average global mean recovery times of 36 years (see Supplementary Material Tab. S4).

2.2 Methodology

For an extreme climate event i, where $i =$ crop failure, drought, flood, heatwave, tropical cyclone, and wildfire, we denote the binary exposure in the grid cell (θ, ϕ) and in year y by $f_i^{jk}(y, \theta, \phi)$, where j and k signify the driving climate model and impact model, respectively. Since we perform the analysis for each event category, model combination, and grid cell position separately, we simplify the notation by dropping the respective indices and arguments. For investigating changes in extreme event recovery times, we divide the simulation interval $I = 1850 - 2099$ into five equal-size intervals, each of length $\Delta T = 50$ years, namely $1850 - 1899, 1900 - 1949, \ldots, 2050 - 2099$. The window size ΔT is chosen to encompass the expected mean recovery time of piControl from the extreme event definition. Specifically, all six event types are based on a threshold criterion, namely either the 2.5th, 97.5th or 98.8th percentile. The expected recovery times are therefore around 40 years within piControl and expected to decrease through global warming. Only for the stable climate conditions of piControl we use the full interval I and show that the results are robust when comparing to the median over the full 250 years time intervals (see Supplemental Material Sec. 3.2).

For each time interval of length ΔT starting at t_0, we define the mean recovery time as

$$\frac{\Delta T}{\sum_{m=0}^{\Delta T-1} f(t_0 + m)}, \tag{1}$$

which corresponds to the inverse experimental probability of an extreme event within the respective time window. Note that in the case where no extreme event occurs within a time window we say that the mean recovery time is not defined. This definition is equivalent to the average recovery time within a fixed time window under periodic boundary conditions (see Fig. 1).

Note that the assumption of periodic boundary conditions weighs lighter on the mean recovery time with increasing number of extreme events. As an additional aggregated measure for the extreme event exposure we define the *total affected area*

$$A_i = \sum_{\theta,\phi} \sum_{m=0}^{\Delta T-1} f_i(t_0 + m, \theta, \phi) \cdot A(\theta, \phi), \tag{2}$$

where $A(\theta, \phi)$ is the area of the grid cell at position (θ, ϕ). Consequently, A_i measures the total area affected by extreme events of type i, respectively, in the time window t_0 to $t_0 + \Delta T$.

2.3 Result aggregation

The ISIMIP multi-model framework allows to calculate the variance from different model combinations and deduce more robust estimates for the mean recovery time. This variation from climate and impact model combinations is due to different modeling assumptions, leading to differences in the corresponding extreme event time series. Our estimate is based on the median over all model combinations where a mean recovery time is defined. If no extreme event occurs within a time window for

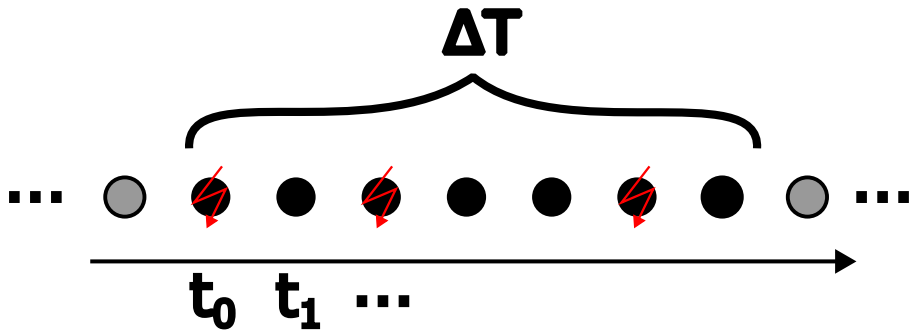


Figure 1: Graphical representation of the mean recovery time. The time series is denoted as black circles at time steps t_0, t_1, ... within a time window of length ΔT. The gray filling denotes sections of the time series outside the time window. The mean recovery time for extreme event occurrences (red arrows) is defined as the ratio between ΔT and the number of extreme events which equals $7/3$ in our example. This is equivalent to the average recovery times under periodic boundary conditions, namely $(2+3+2)/3$, where 2 years pass between the first extreme event and the second, 3 years pass between the second and the third event, and 2 years pass between the third and first event (periodic boundary conditions).

all climate-impact model combination, we are unable to define a multi-model median mean recovery time. The number of mean recovery time detecting models is in general larger than one for SSP1-2.6 and time window 2050–2099 (see Supplementary Information Sec. 5). We discuss the regional differences of detecting models in Sec. 3.

The median is applied separately to each scenario, time window, and grid cell location. Our approach helps to account for potential instabilities in mean recovery time estimation due to time series sampling issues (see Fig. 2).

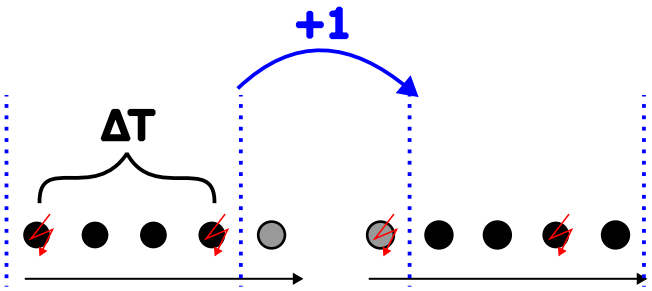


Figure 2: Graphical representation of sampling issues that occur if the time window (blue dotted line) is shifted by a single year. While the left time windows perfectly encompasses two extreme event occurrences with a recovery time of 2 years, we end up with only one impact occurrence in the shifted time window (right). Therefore, the recovery time doubles to 4 years.

We find that the standard deviation ranges between 0.2 and 4 years for the piControl global mean recovery times (see Supplementary Information Sec. 3.1). These deviations arise from the sampling issue described above and the definition of the extreme event. For example, the largest standard deviation of 4 years appears in crop failure where different crop combinations may lead to the failure of more than 30% of the total agricultural area.

On the other hand, within the SSP1-2.6 scenario and time window 2050–2099 we find an increase in standard deviation of the global mean recovery time, where values range from 2 to 6 years are observed (see Supplementary Information Sec. 3.3). This increase is mainly based on the differences between impact models (compare Fig. 4).

3 Results

In this study we define extreme events through thresholds based on percentiles of a pre-industrial reference distribution of indicators such as crop yield, soil moisture, flood depth, heat magnitude, wind speed, and burnt area. By definition of the extreme events we observe median global mean recovery times strongly concentrated around 36 years when calculating the pre-industrial mean recovery time over the whole simulation interval $I = 1850 - 2100$ for drought, heatwave, tropical cyclones, and wildfire (see Supplemental Material Sec. 3.1). This number aligns with the expected mean recovery time for an event with probability 2.5% within a 250y time interval, namely an expected number of event of 6.25 which corresponds to a recovery time between $250/7 \approx 35.7$ and $250/6 \approx 41.7$ years. In the case of flood events we observe a wider distribution of mean recovery times related to larger differences to the expected 36 years, namely a median global mean recovery time of 34 years with a standard deviation of 4 years. This difference is based on the four different crops that are either irrigated or not and fail independently from each other. As crop failure within a grid cell is defined as the failure for at least 30% of the crop land, we observe differences in mean recovery time depending on land use (see Supplemental Material Sec. 3.1).

We investigate the change in mean recovery times as a function of global warming by reducing the time window widths to $\Delta T = 50$ years and calculating the mean recovery times for the SSP scenarios SSP1-2.6, SSP3-7.0, and SSP5-8.5. The time window of 50y is sufficient to encompass the observed mean recovery times from the piControl run which are expected to shrink under historical conditions and future scenarios. The warming level for each climate model and SSP scenario is defined as the difference between the bias-corrected annual mean near-surface air temperature and the respective piControl temperature average over the time range 1841–2100. Since we calculate mean recovery times for time windows we define the global warming level within a time window to equal the average over yearly global warming levels within the time window. Across all event categories we observe a drop from previously large mean recovery times observed in piControl as a function of global warming (see Fig. 3).

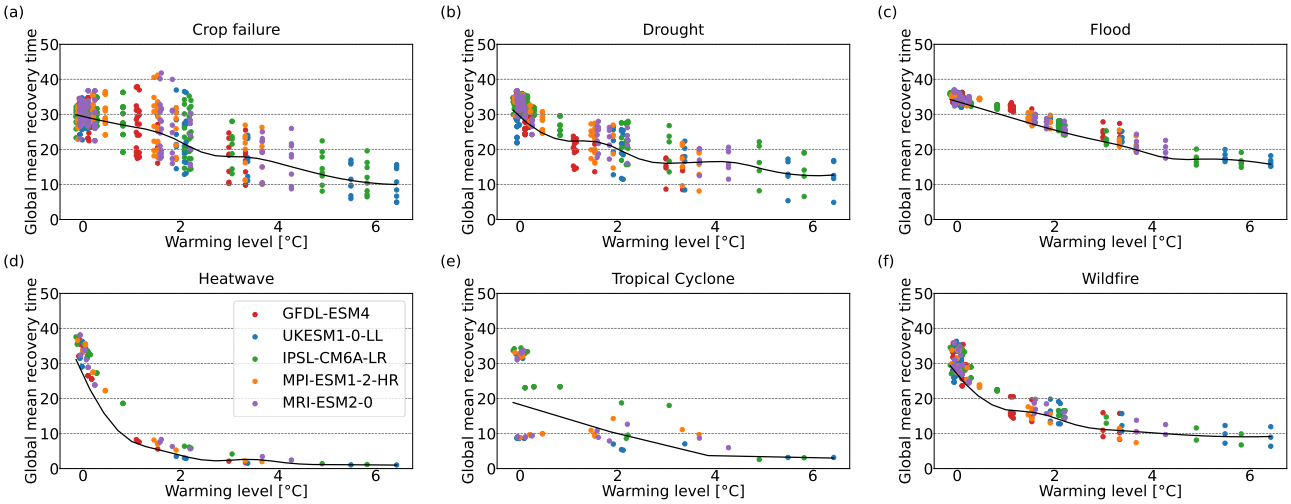


Figure 3: Average global mean recovery time for (a) crop failure, (b) drought, (c) flood, (d) heatwave, (e) tropical cyclone and (f) wildfire. The average value is an area weighted mean while the warming level is calculated from annual mean near-surface temperature given by the SSP scenarios with respect to the piControl annual mean near-surface temperature. The black line shows a quadratic spline as a guide to the eye while for tropical cyclones we use linear interpolation due to the large variance.

Note that average global mean recovery times for $\Delta T = 50$ years are smaller than the respective piControl results for $\Delta T = 250$ years in the cases where the warming level is close to zero. The small difference of 1 to 4 years in the median values applies to all event categories (see Supplementary

Material Sec. 3.1). This reduced value is due to the smaller window size leading to artificially smaller mean recovery times within piControl (see Supplemental Material Sec. 3.2). In addition, we find a broad range of mean recovery times between 10 and 35 years around zero warming levels in the case of tropical cyclones where the cluster at the lower end (see Fig. 3 (e)) stems from early historical simulations.

The decrease in global mean recovery time as a function of global warming applies to all impact categories but differs in its specific form. While crop failure, and floods exhibit a rather linear decay between 0 and 6°C warming we find strong decay at low warming levels for drought, heatwave, and wildfire that level out at larger temperatures in the quadratic spline interpolation (see Fig. 3). Specifically, in the case of heatwaves and wildfires we observe a strong decrease in global mean recovery time between 0 and 1°C warming. In the case of tropical cyclones we observe a reduction in mean recovery time with a large variance based on fewer climate models which leads to additional fluctuations in the spline interpolation (see Fig. 3 (e)). The crop failure recovery time fans out up to a warming level of close to 2°C partly exceeding the respective piControl mean recovery time. This is consistent with the large variance in global crop productivity across models [50]. We find a similar warming dependency of mean recovery time across event types also in observation-based climatic conditions as processed within the ISIMIP3 setup [19, 20] (see Supplementary Information Sec. 2).

These differences in global mean recovery times are also reflected in the total area affected by extreme events in a moving 50 years window (see Eq. (2)) calculated for historical and future SSP1-2.6 simulations (see Fig. 4).

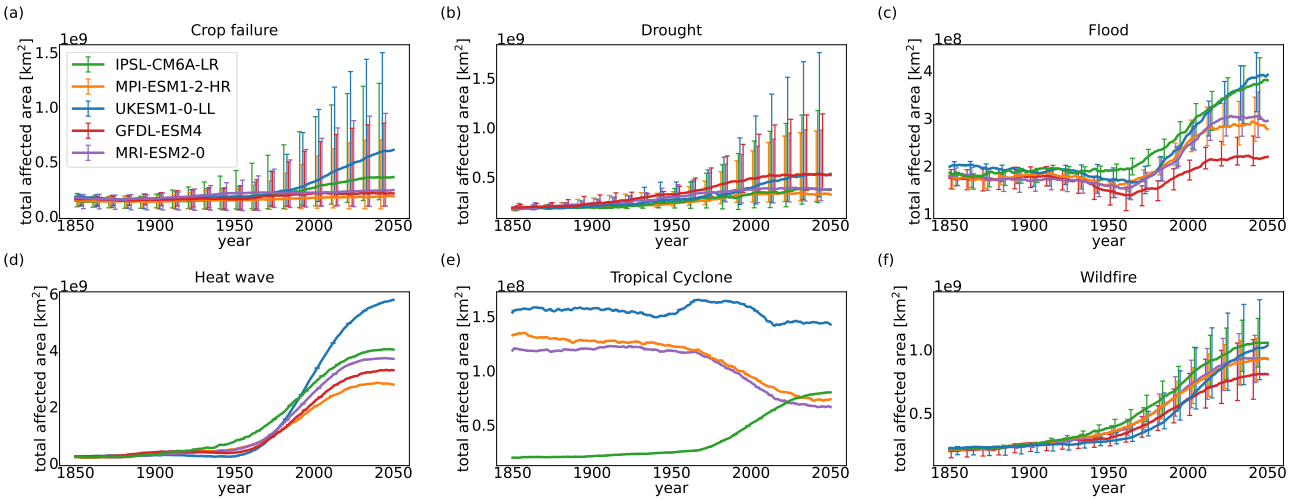


Figure 4: Total global area affected by (a) crop failure, (b) drought, (c) flood, (d) heatwave, (e) tropical cyclone, and (f) wildfire accumulated within a moving 50 years time interval (see Eq. 2) for SSP1-2.6. The colored lines show the median value in units of km^2 over all impact models for each GCM. The error bars show the range along different impact models (not applicable for heatwave and tropical cyclone), where we show only every tenth bar for visibility.

While median crop failure, drought, flood, and tropical cyclone exposure remains limited to the order of magnitude of 100 million square kilometers or below we find that the other event categories pass the 1 billion square kilometers mark at later times. Note that the transition towards larger affected areas occurs around 1950 for all impact categories. At the end of the century all event categories exhibit a saturation in total affected area due to the stabilization of the global warming within SSP1-2.6. In the case of tropical cyclones we observe a reduction in total affected area for two GCMs, namely MPI-ESM1-2-HR and MRI-ESM2-0, as a function of time. This qualitative difference is related to the non-linear response within the tropical cyclone model where minor variations in near-surface temperature and ENSO index between GCMs may result in large changes in the tropical cyclone trajectory and wind speed (see Supplementary Information Sec. 4). For SSP3-7.0 and SSP5-

8.5 we find dominantly increasing trends of total affected area as a function of time due to the stronger warming trend; specifically, we find increasing tropical cyclone affected areas for MRI-ESM2-0 and SSP5-8.5 in contrast to the SSP1-2.6 results presented here (see Supplementary Information Sec. 8).

Even in the mild warming scenario SSP1-2.6 we find strong regional differences in mean recovery time for the time window $2050 - 2099$ (see Fig. 5 and Fig. 6). The spatial heterogeneity in mean recovery times of crop failure, drought, flood, and tropical cyclone leads to a smaller decay in global mean recovery time as compared to the respective mean recovery times for heatwave and wildfire (compare Fig. 3). An explicit visualization of the difference mean recovery time between SSP1-2.6 and piControl results for the time window 2050–2100 is shown in Supplementary Information Sec. 7.

In the case of crop failure we find that most drastic shifts towards smallest mean recovery time occur at low latitudes (see Fig. 5 (a)). These findings are consistent with projected crop yield studies where regional differences arise from water availability, temperature, and crop type [51]. Especially in the Americas and central Africa we find large clusters where extreme events occur at a high frequency corresponding to lowest mean recovery times. On the other hand, we find large areas at high latitudes with large recovery times in extended parts of southern Africa, central Asia and Australia (dark blue). The mean recovery time even exceeds the median picontral mean recovery of 36 years indicating improved crop conditions at intermediate warming. Note that the low latitude results are accompanied by large model variances in these regions (see Supplementary Material Sec. 6). Such latitude effects on crop yields were attributed to CO_2 fertilization effects and crop type [51, 52]. This observation also aligns with the global mean recovery time at low warming levels (compare Fig. 3 (a)).

For droughts we find smallest mean recovery times in the Boreal Forest Area, the Mediterranean, Central and South-East Asia, the Brazilian and the Appalachian Highlands (see Fig. 5 (b)). In contrast, we find extensive areas in central and southern Asia, eastern Africa, northern Australia, and the Pampa with largest mean recovery times of 45 to 50 years. This observation signifies improved soil moisture conditions represented by mean recovery times exceeding the piControl reference. Note that especially in Asia and both Americas we find a large variance in mean recovery time from the different models (see Supplementary Material Sec. 6). Our findings are consistent with similar studies on soil moisture changes that also highlight the large variance across models [53–56].

Floods show no shifts to smallest recovery times and moderate changes overall (see Fig. 5 (c)). Only in central Africa, Asia, the Amazon and both Americas we find extended clusters where recovery times are below 20 years. On the other hand, we again find regions, e.g. central America, South Africa, Australia, and Eastern Europe, where mean recovery times exceed the expected piControl mean recovery times. These results are consistent with 100-year floods results from CMIP6 [57, 58].

Heatwaves as defined through the HWMId indicator are projected to occur yearly almost everywhere at low latitudes but even in large segments of central Asia and North America (see Fig. 6 (a)). For the rest of the world we observe mean recovery times that are only a few years in contrast to the median piControl value of 36 years. These results are also reflected in the strong decay of global mean recovery time where the number decreases to below 10 years close to the 2°C warming level. (see Fig. 3 (d)). Note that these mean recovery times show large model variance centered around 10–15 years (see Supplementary Material Sec. 6). This large variance of heatwaves across models was previously reported for the CMIP6 simulations [59].

In general, the event frequency of tropical cyclones increases compared to the piControl value. Only in Australia we find clusters of mean recovery times with values between 45 and 50 years as compared to the expected pre-industrial value of 36 years. Note that these results show a large model variance in the Americas and east Asia (see Supplementary Material Sec. 6) while only few models detect extreme tropical cyclones in South Asia (see Supplementary Material Sec. 5). This high sensitivity of tropical cyclone results has been previously reported [60, 61]. A study on extreme tropical cyclones suggests regional differences in frequency changes due to warming where both increases and decreases are projected [62].

For wildfires we find a heterogeneous picture of mean recovery times where large clusters of

smallest recovery times below five years appear in the Sahel region and Southern Africa, the Mediterranean, Central Asia, and both Americas (see Fig. 6 (c)). Note that the model variance of mean recovery times for central Asia is above 15 years (see Supplementary Material Sec. 6) and only half of the models detect extreme wildfires in the time windows 2050–2099 (see Supplementary Material Sec. 5). Other world regions experience a smaller reduction in mean recovery times but around 90% of the affected areas have mean recovery times of below 25 years. This global trend is reflected in the decay of global mean recovery times even for small levels of global warming (compare Fig. 3 (f)). Our results are consistent with increases in burnt area fraction projections [63, 64].

4 Discussion

We have investigated mean recovery times and affected areas for harmonized extreme event projections across six categories, namely crop failure, drought, heatwave, flood, tropical cyclone and wildfire.

Our results on global mean recovery times are consistent with the previous generation of ISIMIP-derived extreme event projections in terms of increasing land area exposure and main features of geographical exposure [2]. Only in the case of floods and tropical cyclones we observe qualitative strong differences, namely regional trends of exposure as a function of warming. Note that a strict comparison is not meaningful due to the differences in extreme event definitions. For example, floods are based on 40-year return levels while the extreme flood definition in Ref. [2] applies 100-year return levels which have been shown to respond differently to global warming [14]. Similarly, tropical cyclones in Ref. [2] were based on a different tropical cyclone definition, namely the mean number of tropical cyclone track realizations without pre-industrial percentile threshold.

Previous studies on crop yield and crop failure also find both positive and negative effects within the model variance at weak global warming which are attributed for example to model-specific crop processes and CO_2 fertilization [2, 50, 65–67]. Nonetheless, these effects do not offset the average decline in crop yield at higher global warming which we also find in this study. Furthermore, the large variance arising from the different crop processes [67] also translates into large variances in our results.

In the case of extreme drought global hydrological models were observed to have a drying bias [68] which may lead to overestimated drought events in our analysis. Uncertainties for drought estimation were previously attributed to mainly the global hydrological models but with additional significant contributions from the GCMs. [53]

Extreme flood events are difficult to represent within global hydrological models as both low-flow and high-flow conditions are not well captured [69]. While the additional discharge routing within Cama-Flood can improve on the results of some global hydrological models the peak discharge is generally overestimated [13]. Consequently, the small variance arising from the impact models observed in this study may conceal the actual uncertainty within extreme flood events [70]. In addition, the choice of return level can highly influence the respective event probability and its dependence on global warming [14]. Especially, the choice of reference period for fitting to the generalized extreme value distribution and estimating return periods has a strong influence on the flood frequency results that may be falsely attributed to global warming [71].

While our extended extreme heatwave results are consistent with increased warming there is specific additional uncertainty in regional hot spots which may be underestimated due to nonlinear couplings [72]. Note that the non-linear increases in extreme heat are already observed in historical heatwaves with exponential increases in frequency [73]. Our study finds qualitatively similar non-linear warming trends both in exposed area and mean recovery time.

Uncertainties for wildfire modeling are observed in similar studies where especially direct human influences such as fire management, ignition, and suppression are important factors [32, 74]. This

missing aspects lead to an imbalance between projected increases in burnt area while historical observations point in the opposite direction. Nevertheless, global warming has increased the frequency of extreme wildfires globally [75, 76] consistent with our findings.

Tropical cyclone projections span a wide range from increasing [77] to decreasing frequencies [61]. The differences arise from the internal variability of the GCMs to which tropical cyclones are sensitive [78]. Our findings show similarly a large variance across models and SSP scenarios.

Conflict of interest statement

All authors declare that they have no conflicts of interest.

Author contribution

K.Z. and J.S. designed the research and developed the methodology. K.Z. performed the analysis. The interpretation of the results was done by K.Z., J.S., and D.Q.-C. K.Z. wrote the manuscript. D.-Q.-C., S.Z., J.V., K.F., and J.S. contributed and/or coordinated model experiments. D.Q.-C., S.Z., J.V., and J.S. contributed to the manuscript review and editing. K.Z., D.Q.-C., S.Z., J.V., K.F., and J.S. were involved in the production of the extreme event impact data.

Acknowledgments

This work used resources of the Deutsches Klimarechenzentrum (DKRZ) granted by its Scientific Steering Committee (WLA) under project bb0820. KZ was financially supported through the European Union Horizon 2020 programme (HABITABLE project (Grant 869395)). SZ, DQC and JS were financially supported by the European Union Horizon Europe programme, grant number 101137673.

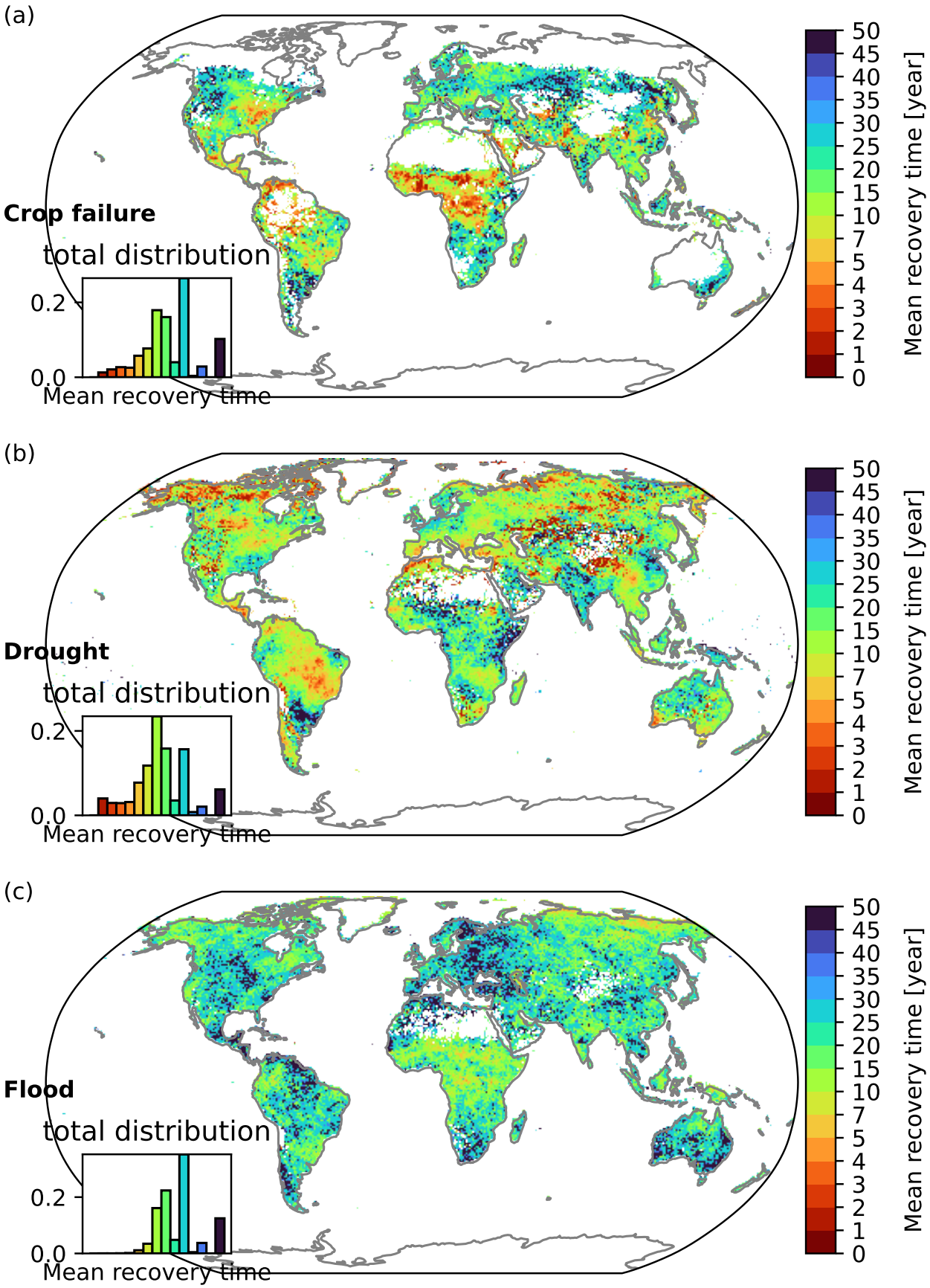


Figure 5: Multi-model median mean recovery times for (a) crop failure, (b) drought, and (c) flood for SSP1-2.6 and the time window 2050 – 2099. Mean recovery times are grouped in intervals ranging from 0–1 years (red-brown) to 45–50 years (black). The inset shows the distribution of the mean recovery time counts.

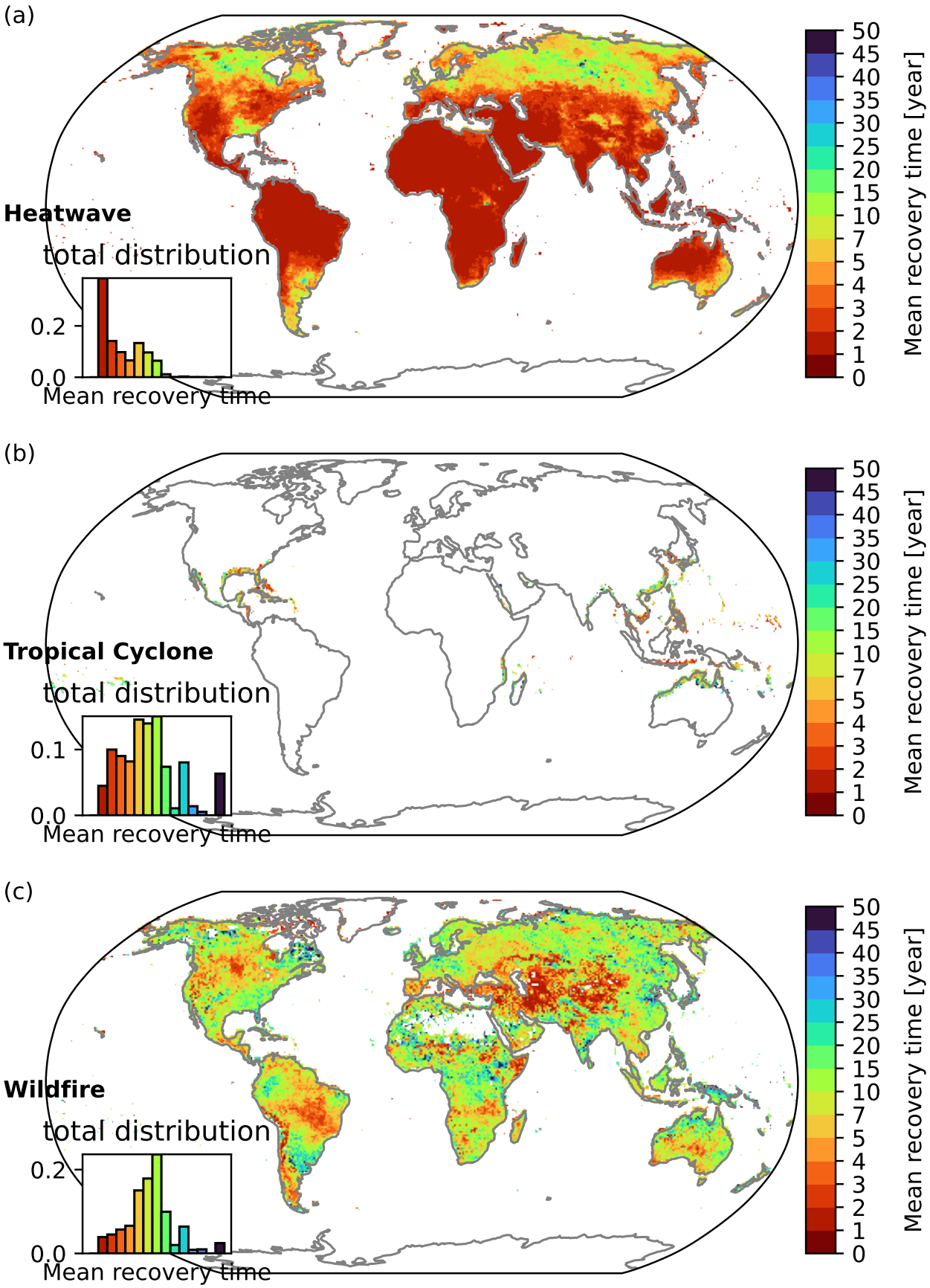


Figure 6: Multi-model median mean recovery times for (a) heatwave, (b) tropical cyclone, and (c) wildfire for SSP1-2.6 and the time window 2050 – 2099. Mean recovery times are grouped in intervals ranging from 0–1 years (red-brown) to 45–50 years (black). The inset shows the distribution of the mean recovery time counts.

References

1. Easterling, D. R. *et al.* Climate Extremes: Observations, Modeling, and Impacts. *Science* **289,** 2068–2074 (2000).
2. Lange, S. *et al.* Projecting Exposure to Extreme Climate Impact Events Across Six Event Categories and Three Spatial Scales. *Earth's Future* **8.** e2020EF001616 10.1029/2020EF001616, e2020EF001616 (2020).
3. O'Neill, B. *et al.* in *Climate Change 2022: Impacts, Adaptation and Vulnerability. Contribution of Working Group II to the Sixth Assessment Report of the Intergovernmental Panel on Climate Change* (eds Pörtner, H.-O. *et al.*) 2411–2538 (Cambridge University Press, Cambridge, UK and New York, NY, USA, 2022).
4. Douris, J. & Kim, G. The Atlas of Mortality and Economic Losses from Weather, Climate and Water Extremes (1970-2019). *WMO* (2021).
5. IDMC. Global Report on Internal Displacement 2025 (2025).
6. Beniston, M. *et al.* Future extreme events in European climate: an exploration of regional climate model projections. *Climatic Change* **81,** 71–95 (2007).
7. Gershunov, A. *et al.* in *Assessment of climate change in the southwest United States: a report prepared for the National Climate Assessment* 126–147 (Springer, 2013).
8. Thiery, W. *et al.* Intergenerational inequities in exposure to climate extremes. *Science* **374,** 158–160 (2021).
9. Zantout, K. *et al.* Shifting dominant periods in extreme climate impacts under global warming. *Nature Communications* **16,** 9746 (2025).
10. Gaupp, F., Hall, J., Hochrainer-Stigler, S. & Dadson, S. Changing risks of simultaneous global breadbasket failure. *Nature Climate Change* **10,** 54–57 (2020).
11. Jägermeyr, J. *et al.* Climate impacts on global agriculture emerge earlier in new generation of climate and crop models. *Nature Food* **2,** 873–885 (2021).
12. Brunner, L. & Voigt, A. Pitfalls in diagnosing temperature extremes. *Nature Communications* **15,** 2087 (2024).
13. Heinicke, S. *et al.* Global hydrological models continue to overestimate river discharge. *Environmental Research Letters* **19,** 074005 (2024).
14. Slater, L. *et al.* Global Changes in 20-Year, 50-Year, and 100-Year River Floods. *Geophysical Research Letters* **48.** e2020GL091824 2020GL091824, e2020GL091824 (2021).
15. Van Langevelde, F. *et al.* EFFECTS OF FIRE AND HERBIVORY ON THE STABILITY OF SAVANNA ECOSYSTEMS. *Ecology* **84,** 337–350 (2003).
16. Osborne, K. *et al.* Delayed coral recovery in a warming ocean. *Global Change Biology* **23,** 3869–3881 (2017).
17. Fairman, T. A., Nitschke, C. R. & Bennett, L. T. Too much, too soon? A review of the effects of increasing wildfire frequency on tree mortality and regeneration in temperate eucalypt forests. *International Journal of Wildland Fire* **25,** 831–848 (2016).
18. Turner, M. G., Braziunas, K. H., Hansen, W. D. & Harvey, B. J. Short-interval severe fire erodes the resilience of subalpine lodgepole pine forests. *Proceedings of the National Academy of Sciences* **116,** 11319–11328 (2019).
19. Frieler, K. *et al.* Scenario setup and forcing data for impact model evaluation and impact attribution within the third round of the Inter-Sectoral Impact Model Intercomparison Project (ISIMIP3a). *Geoscientific Model Development* **17,** 1–51 (2024).

20. Frieler, K. *et al.* Scenario set-up and the new CMIP6-based climate-related forcings provided within the third round of the Inter-Sectoral Model Intercomparison Project (ISIMIP3b, group I and II). *EGUsphere* **2025,** 1–70 (2025).

21. ISIMIP3. https://www.isimip.org/protocol/3/ (2024).

22. Caparas, M., Zobel, Z., Castanho, A. D. A. & Schwalm, C. R. Increasing risks of crop failure and water scarcity in global breadbaskets by 2030. *Environmental Research Letters* **16,** 104013 (2021).

23. Zhu, P. *et al.* Warming reduces global agricultural production by decreasing cropping frequency and yields. *Nature Climate Change* **12,** 1016–1023 (2022).

24. Chiang, F., Mazdiyasni, O. & AghaKouchak, A. Evidence of anthropogenic impacts on global drought frequency, duration, and intensity. *Nature Communications* **12,** 2754 (2021).

25. Whitfield, P. Floods in future climates: a review. *Journal of Flood Risk Management* **5,** 336–365 (2012).

26. Perkins-Kirkpatrick, S. E. & Gibson, P. B. Changes in regional heatwave characteristics as a function of increasing global temperature. *Scientific Reports* **7,** 12256 (2017).

27. Stocker, T. *Climate change 2013: the physical science basis: Working Group I contribution to the Fifth assessment report of the Intergovernmental Panel on Climate Change* (Cambridge university press, 2014).

28. Walsh, K. J. *et al.* Tropical cyclones and climate change. *WIREs Climate Change* **7,** 65–89 (2016).

29. Sobel, A. H. *et al.* Tropical Cyclone Frequency. *Earth's Future* **9,** e2021EF002275 (2021).

30. Jones, M. W. *et al.* Global and Regional Trends and Drivers of Fire Under Climate Change. *Reviews of Geophysics* **60.** e2020RG000726 2020RG000726, e2020RG000726 (2022).

31. Lobell, D. B., Schlenker, W. & Costa-Roberts, J. Climate Trends and Global Crop Production Since 1980. *Science* **333,** 616–620 (2011).

32. Andela, N. *et al.* A human-driven decline in global burned area. *Science* **356,** 1356–1362 (2017).

33. Sheridan, S. C. & Allen, M. J. Temporal trends in human vulnerability to excessive heat. *Environmental Research Letters* **13,** 043001 (2018).

34. Zhang, A. Y., Bennett, M. B., Martin, S. & Grow, H. M. Climate Change and Heat: Challenges for Child Health Outcomes and Inequities. *Current Pediatrics Reports* (2024).

35. Buhaug, H. & Vestby, J. On Growth Projections in the Shared Socioeconomic Pathways. *Global Environmental Politics* **19,** 118–132 (Nov. 2019).

36. Lange, S. Trend-preserving bias adjustment and statistical downscaling with ISIMIP3BASD (v1.0). *Geoscientific Model Development* **12,** 3055–3070 (2019).

37. Lange, S. *ISIMIP3BASD* version 2.5.0 (Zenodo, Apr. 2021).

38. Eyring, V. *et al.* Overview of the Coupled Model Intercomparison Project Phase 6 (CMIP6) experimental design and organization. *Geoscientific Model Development* **9,** 1937–1958 (2016).

39. Tebaldi, C. *et al.* Climate model projections from the Scenario Model Intercomparison Project (ScenarioMIP) of CMIP6. *Earth System Dynamics* **12,** 253–293 (2021).

40. Van Vuuren, D. P. & Carter, T. R. Climate and socio-economic scenarios for climate change research and assessment: reconciling the new with the old. *Climatic Change* **122,** 415–429 (2014).

41. Van Vuuren, D. P. *et al.* A new scenario framework for Climate Change Research: scenario matrix architecture. *Climatic Change* **122,** 373–386 (2014).

42. Yamazaki, D., Kanae, S., Kim, H. & Oki, T. A physically based description of floodplain inundation dynamics in a global river routing model. *Water Resources Research* **47** (2011).

43. Emanuel, K., Sundararajan, R. & Williams, J. Hurricanes and Global Warming: Results from Downscaling IPCC AR4 Simulations. *Bulletin of the American Meteorological Society* **89,** 347–368 (Mar. 2008).

44. Emanuel, K. A. Downscaling CMIP5 climate models shows increased tropical cyclone activity over the 21st century. *Proceedings of the National Academy of Sciences* **110,** 12219–12224 (2013).

45. Holland, G. A Revised Hurricane Pressure–Wind Model. *Monthly Weather Review* **136,** 3432–3445 (Sept. 2008).

46. Knapp, K. R., Kruk, M. C., Levinson, D. H., Diamond, H. J. & Neumann, C. J. The International Best Track Archive for Climate Stewardship (IBTrACS): Unifying Tropical Cyclone Data. *Bulletin of the American Meteorological Society* **91,** 363–376 (Mar. 2010).

47. Geiger, T., Gütschow, J., Bresch, D. N., Emanuel, K. & Frieler, K. Double benefit of limiting global warming for tropical cyclone exposure. *Nature Climate Change* **11,** 861–866 (Oct. 2021).

48. Russo, S., Sillmann, J. & Fischer, E. M. Top ten European heatwaves since 1950 and their occurrence in the coming decades. *Environmental Research Letters* **10,** 124003 (2015).

49. Russo, S., Sillmann, J. & Sterl, A. Humid heat waves at different warming levels. *Scientific Reports* **7,** 7477 (2017).

50. Müller, C. *et al.* Exploring uncertainties in global crop yield projections in a large ensemble of crop models and CMIP5 and CMIP6 climate scenarios. *Environmental Research Letters* **16,** 034040 (2021).

51. Rezaei, E. E. *et al.* Climate change impacts on crop yields. *Nature Reviews Earth & Environment* **4,** 831–846 (2023).

52. McGrath, J. M. & Lobell, D. B. Regional disparities in the CO2 fertilization effect and implications for crop yields. *Environmental Research Letters* **8,** 014054 (2013).

53. Prudhomme, C. *et al.* Hydrological droughts in the 21st century, hotspots and uncertainties from a global multimodel ensemble experiment. *Proceedings of the National Academy of Sciences* **111,** 3262–3267 (2014).

54. Berg, A., Sheffield, J. & Milly, P. C. D. Divergent surface and total soil moisture projections under global warming. *Geophysical Research Letters* **44,** 236–244 (2017).

55. Cheng, S., Huang, J., Ji, F. & Lin, L. Uncertainties of soil moisture in historical simulations and future projections. *Journal of Geophysical Research: Atmospheres* **122,** 2239–2253 (2017).

56. Yao, L. *et al.* Emergent constraints on global soil moisture projections under climate change. *Communications Earth & Environment* **6,** 39 (2025).

57. Hirabayashi, Y. *et al.* Global flood risk under climate change. *Nature Climate Change* **3,** 816–821 (2013).

58. Hirabayashi, Y., Tanoue, M., Sasaki, O., Zhou, X. & Yamazaki, D. Global exposure to flooding from the new CMIP6 climate model projections. *Scientific Reports* **11,** 3740 (2021).

59. Al-Yaari, A., Zhao, Y., Cheruy, F. & Thiery, W. Heatwave Characteristics in the Recent Climate and at Different Global Warming Levels: A Multimodel Analysis at the Global Scale. *Earth's Future* **11.** e2022EF003301 2022EF003301, e2022EF003301 (2023).

60. Knutson, T. R. *et al.* Tropical cyclones and climate change. *Nature Geoscience* **3,** 157–163 (2010).

61. Lee, C.-Y., Camargo, S. J., Sobel, A. H. & Tippett, M. K. Statistical–Dynamical Downscaling Projections of Tropical Cyclone Activity in a Warming Climate: Two Diverging Genesis Scenarios. *Journal of Climate* **33,** 4815 –4834 (2020).

62. Sugi, M., Murakami, H. & Yoshida, K. Projection of future changes in the frequency of intense tropical cyclones. *Climate Dynamics* **49,** 619–632 (2017).

63. Bowman, D. M. J. S. *et al.* Human exposure and sensitivity to globally extreme wildfire events. *Nature Ecology & Evolution* **1,** 0058 (2017).

64. Peng, X. *et al.* Projections of wildfire risk and activities under 1.5 °C and 2.0 °C global warming scenarios. *Environmental Research Communications* **5,** 031002 (2023).

65. Schleussner, C.-F. *et al.* Crop productivity changes in 1.5°C and 2°C worlds under climate sensitivity uncertainty. *Environmental Research Letters* **13,** 064007 (2018).

66. Minoli, S. *et al.* Global Response Patterns of Major Rainfed Crops to Adaptation by Maintaining Current Growing Periods and Irrigation. *Earth's Future* **7,** 1464–1480 (2019).

67. Müller, C. *et al.* Substantial Differences in Crop Yield Sensitivities Between Models Call for Functionality-Based Model Evaluation. *Earth's Future* **12.** e2023EF003773 2023EF003773, e2023EF003773 (2024).

68. Milly, P. & Dunne, K. A. A Hydrologic Drying Bias in Water-Resource Impact Analyses of Anthropogenic Climate Change. *JAWRA Journal of the American Water Resources Association* **53,** 822–838 (2017).

69. Do, H. X. *et al.* Historical and future changes in global flood magnitude – evidence from a model–observation investigation. *Hydrology and Earth System Sciences* **24,** 1543–1564 (2020).

70. Mester, B., Willner, S. N., Frieler, K. & Schewe, J. Evaluation of river flood extent simulated with multiple global hydrological models and climate forcings. *Environmental Research Letters* **16,** 094010 (2021).

71. Zhao, F., Lange, S., Goswami, B. & Frieler, K. Frequency Bias Causes Overestimation of Climate Change Impacts on Global Flood Occurrence. *Geophysical Research Letters* **51.** e2024GL108855 2024GL108855, e2024GL108855 (2024).

72. Kornhuber, K., Bartusek, S., Seager, R., Schellnhuber, H. J. & Ting, M. Global emergence of regional heatwave hotspots outpaces climate model simulations. *Proceedings of the National Academy of Sciences* **121,** e2411258121 (2024).

73. Vautard, R. *et al.* Heat extremes linearly shift with global warming, with frequency doubling per decade since 1979. *Environmental Research Letters* **19,** 094033 (2024).

74. Forkel, M. *et al.* Emergent relationships with respect to burned area in global satellite observations and fire-enabled vegetation models. *Biogeosciences* **16,** 57–76 (2019).

75. Burton, C. *et al.* Global burned area increasingly explained by climate change. *Nature Climate Change* **14,** 1186–1192 (2024).

76. Abatzoglou, J. T. *et al.* Climate change has increased the odds of extreme regional forest fire years globally. *Nature Communications* **16,** 6390 (2025).

77. Wehner, M. F., Reed, K. A., Loring, B., Stone, D. & Krishnan, H. Changes in tropical cyclones under stabilized 1.5 and 2.0°C global warming scenarios as simulated by the Community Atmospheric Model under the HAPPI protocols. *Earth System Dynamics* **9,** 187–195 (2018).

78. Gettelman, A., Bresch, D. N., Chen, C. C., Truesdale, J. E. & Bacmeister, J. T. Projections of future tropical cyclone damage with a high-resolution global climate model. *Climatic Change* **146,** 575–585 (2018).

Supplementary Files

This is a list of supplementary files associated with this preprint. Click to download.

- mainsupplement.pdf